Synchronous Reluctance Motor Parameter and State Estimation Using Extended Kalman Filter and Current Derivative Measurement

Zbynek Mynar ®, *Member, IEEE*, Pavel Vaclavek ®, *Senior Member, IEEE*, and Petr Blaha ®

Abstract—**The synchronous reluctance motor is becoming a very attractive alternative to the ac induction machine. This is due to the lack of rare-earth metals in their construction and a higher efficiency, which was brought about by recent progress in rotor design. However, in order to achieve an efficient and low-cost operation of the synchronous reluctance motor drive, an adaptive sensorless algorithm should be utilized to cope with machine nonlinearities. This article describes an adaptive observer, which can provide an estimation of rotor position and speed, as well as core loss and inductance parameters. A modified pulsewidth modulation (PWM) switching scheme and a current derivative measurement method are proposed, together with an extended Kalman Filter design. Experimental results are shown to demonstrate the method performance and feasibility.**

Index Terms—**Current derivative, extended Kalman filter (EKF), online adaptive observer, pulsewidth modulation (PWM) excitation, sensorless control, synchronous reluctance motor, synchronous reluctance machine (SynRM).**

I. INTRODUCTION

THE concept of the synchronous reluctance machine (SynRM) dates to the beginning of the previous century, however, only in recent years is gaining more attention. Despite advantages such as its low cost, simple, and rugged construction, cold rotor, a wide field-weakening range and the absence of expensive rare-earth metals, only recent progress in rotor high-anisotropy design has allowed the SynRM to achieve a better efficiency [1], [2]. In fact, it is becoming an attractive

replacement for the ac induction machine in many industrial applications such as pumps or HVACs [3]–[6].

The classical SynRM control method is based on cascaded field-oriented vector control (FOC) [7], [8]. Despite numerous advantages, the SynRM exhibits significant nonlinearity in the form of magnetic saturation, making its power-optimal and preferably sensorless FOC complicated.

There are two major types of SynRM power optimization control algorithms in the literature [9]. The search-type controllers do not require knowledge of machine parameters, however, they usually involve test signal injection and significant convergence time [10]. The second class are the loss model-based methods, which do not exhibit these disadvantages, but they require knowledge of actual machine parameters [11], [12]. This means a relatively complicated offline system identification is needed, or an online adaptive observer, which can provide the necessary information, such as stator inductance, resistance, and core losses [13], [14].

Apart from efficiency optimization, sensorless SynRM control strategies are being extensively investigated. These can be classified based on the operational speed range. Significant rotor anisotropy is exploited by high-frequency injection (HFI) algorithms, which can operate in the low-speed range [15]–[18]. Algorithms based on extended electromotive force (EMF) are then used in the medium-high speed range [19], [20]. Low- and high-speed algorithms are usually either explicitly switched when crossing the speed region, or a hybrid algorithm is employed [21]–[23].

There is clearly a desire for an adaptive observer algorithm, which can provide all the major parameters required for power-efficient sensorless control of a SynRM in the full speed range. Recently, it was shown that simultaneous position, speed, and stator inductance estimation is possible using a fundamental pulsewidth modulation (PWM) excitation and a current derivative measurement [24]. The algorithm proposed in this article combines a similar principle, with a stator flux model suitable for higher speeds using the extended Kalman filter (EKF). The resulting method, described in Section III, can provide position, speed, inductance, core loss, and flux estimations from standstill to the stator voltage limit. An important focus of this article is also the implementation of a reliable current derivative measurement on the SynRM, which usually exhibits large values of stator inductances, thus making precise measurement

Zbynek Mynar is with the Faculty of Electrical Engineering and Communication, Brno University of Technology, 616 00 Brno, Czech Republic (e-mail: xmynar03@stud.feec.vutbr.cz).

Pavel Vaclavek and Petr Blaha are with the Central European Institute of Technology, 61200 Brno, Czechia, and also with Faculty of Electrical Engineering and Communication, Brno University of Technology, 612 00 Brno, Czech Republic (e-mail: pavel.vaclavek@ceitec.vutbr.cz; petr.blaha@ceitec.vutbr.cz).
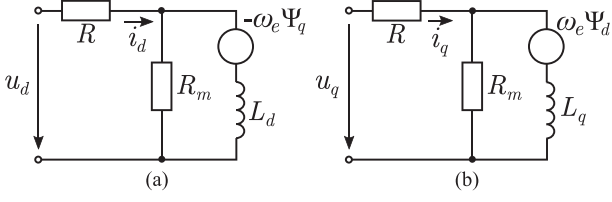
Fig. 1. SynRM model including core losses in (a) direct axis and (b) quadrature axis.

difficult. A modified measurement method and a PWM switching scheme were, therefore, proposed in Sections III-A and III-B. Viability and performance of this approach were proven on a real experimental setup, with results shown in Section IV.

II. SynRM Model Including Core Losses

The model of SynRM in the rotating dq reference frame, which includes core losses, is shown in Fig. 1 and can be expressed as

$$\boldsymbol{u}_{dq} = \begin{bmatrix} R + \omega_e K_m + pL_d & -\omega_e L_q + pK_m \\ \omega_e L_d - pK_m & R + \omega_e K_m + pL_q \end{bmatrix} \boldsymbol{i}_{dq} \quad (1)$$

where $\boldsymbol{i}_{dq} = [i_d, i_q]^{\mathrm{T}}$ is stator current vector, $\boldsymbol{u}_{dq} = [u_d, u_q]^{\mathrm{T}}$ is stator voltage vector, R is stator resistance, ω_e is electrical rotor speed, L_d and L_q are stator direct and quadrature inductances, $K_m = \omega_e L_d L_q / R_m$ is core loss coefficient, R_m is core loss resistance, and p is differential operator [25], [26]. The relation between the measured stator current $\boldsymbol{i}_{dq}$ and stator flux $\boldsymbol{\Psi}_{dq} = [\Psi_d, \Psi_q]^{\mathrm{T}}$ is then

$$\boldsymbol{\Psi}_{dq} = \begin{bmatrix} L_d & K_m \\ -K_m & L_q \end{bmatrix} \boldsymbol{i}_{dq}. \quad (2)$$

The term of normalized reluctance can be introduced for the direct and quadrature axis as

$$\mathcal{R}'_d = \frac{1}{L_d} \text{ and } \mathcal{R}'_q = \frac{1}{L_q}. \quad (3)$$

Combining (1)–(3) leads to the final stator flux model

$$\frac{d\boldsymbol{\Psi}_{dq}}{dt} = \boldsymbol{u}_{dq} - \left\{ \frac{R\mathcal{R}'_d \mathcal{R}'_q}{A} \begin{bmatrix} 1/\mathcal{R}'_q & -K_m \\ K_m & 1/\mathcal{R}'_d \end{bmatrix} + \begin{bmatrix} 0 & -\omega_e \\ \omega_e & 0 \end{bmatrix} \right\} \boldsymbol{\Psi}_{dq} \quad (4)$$

where $A = 1 + K_m^2 \mathcal{R}'_d \mathcal{R}'_q$.

III. Proposed Sensorless Algorithm

The block diagram of the proposed sensorless algorithm is shown in Fig. 2. The normalized reluctances $\mathcal{R}'_{phN}$ of SynRM
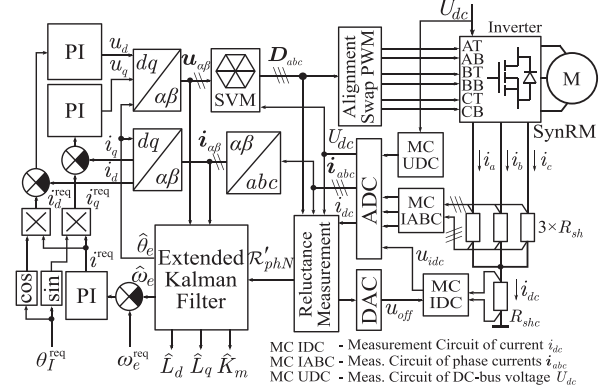

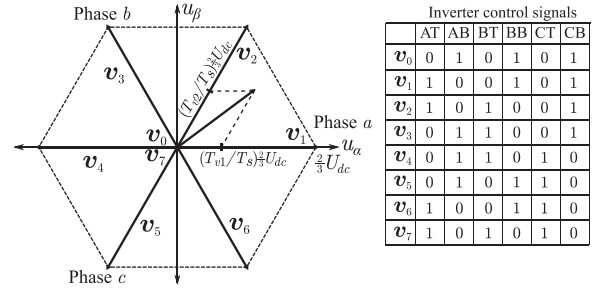Fig. 2. Proposed algorithm in vector control algorithm block diagram.

Fig. 3. Standard SVM voltage generation.

phase $N \in \{a, b, c\}$ are defined similarly to (3) as

$$\mathcal{R}'_{pha} = \frac{1}{L_{pha}} = \mathcal{R}'_d \cos^2(\theta_e) + \mathcal{R}'_q \sin^2(\theta_e)$$

$$\mathcal{R}'_{phb} = \frac{1}{L_{phb}} = \mathcal{R}'_d \cos^2\left(\theta_e + \frac{2\pi}{3}\right) + \mathcal{R}'_q \sin^2\left(\theta_e + \frac{2\pi}{3}\right)$$

$$\mathcal{R}'_{phc} = \frac{1}{L_{phc}} = \mathcal{R}'_d \cos^2\left(\theta_e - \frac{2\pi}{3}\right) + \mathcal{R}'_q \sin^2\left(\theta_e - \frac{2\pi}{3}\right) \quad (5)$$

where L_{pha}, L_{phb}, and L_{phc} are machine phase inductances. The reluctance $\mathcal{R}'_{phN}$ is acquired from the phase current change Δi_{dc} measured at the R_{shc} shunt resistor when one of the nonzero space vector modulation (SVM) voltage vectors $\boldsymbol{v}_M = \{\boldsymbol{v}_1, \boldsymbol{v}_2, \boldsymbol{v}_3, \boldsymbol{v}_4, \boldsymbol{v}_5, \boldsymbol{v}_6\}$ is applied by the inverter for the time duration $\boldsymbol{T}_{vM} = \{T_{v1}, T_{v2}, T_{v3}, T_{v4}, T_{v5}, T_{v6}\}$. The basic principle of SVM is shown in Fig. 3. For example, the phase a normalized reluctance can be obtained during times T_{v1} and T_{v4} as

$$\mathcal{R}'_{pha} \cong \left(\frac{\Delta i_{dc}}{T_{v1}}\right) \frac{1}{\frac{2}{3}U_{dc}} \text{ or } \mathcal{R}'_{pha} \cong \left(\frac{\Delta i_{dc}}{T_{v4}}\right) \frac{1}{\frac{2}{3}U_{dc}} \quad (6)$$

where U_{dc} is the inverter dc-bus voltage. Note that relation (6) was simplified by neglecting the stator resistance R, otherwise the first-order system model would have to be approximated, further increasing computation demands.

In order to provide sufficient torque, stator inductances of the SynRM are usually very large (sometimes hundreds of mH). This significantly complicates the measurement of Δi_{dc} during short periods $\boldsymbol{T}_{vM}$ generated by the standard 10-kHz PWM. For
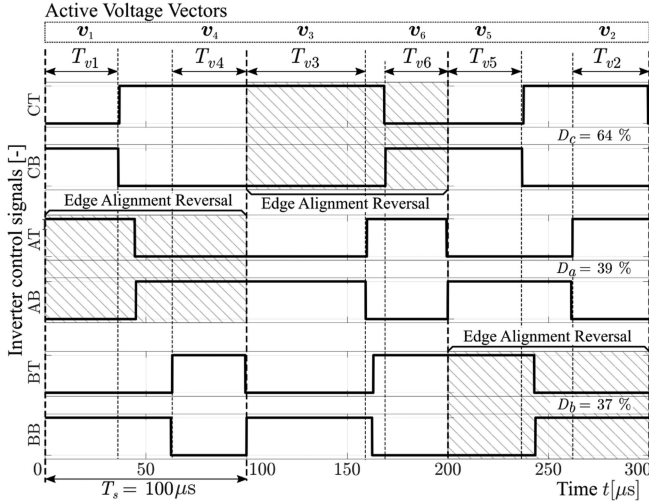
Fig. 4.　Principle of the proposed alignment-swap PWM switching scheme.

Fig. 5.　Measurement circuit of i_{dc} current (MC IDC).

example, with a $\boldsymbol{T}_{vM}$ measurement window of length $T_s/2 = 50\,\mu s$, inverter dc-bus voltage $U_{dc} = 400\,\text{V}$, and the SynRM with $\max(L_d) = 0.5\,\text{H}$, the approximate current change of

$$\min(\Delta i_{dc}) \simeq \frac{T_s \frac{2}{3} U_{dc}}{2\max(L_d)} = \frac{0.0001 \cdot 400}{3 \cdot 0.5} = 26.7\,\text{mA} \quad (7)$$

would have to be measured with sufficient resolution. This requires the introduction of the modified alignment swap PWM switching scheme, which provided improved excitation (described in Section III-A), and Δi_{dc} measurement method, which increased the measurement precision (described in Section III-B).

The EKF presented in Section III-C then uses the acquired $\mathcal{R}'_{phN}$ and stator current measurements to provide estimations of rotor electrical position $\hat{\theta}_e$, electrical angular speed $\hat{\omega}_e$, core loss coefficient $\hat{K}_m$, and stator inductances $\hat{L}_d$ and $\hat{L}_q$. The remaining portion of the algorithm is the commonly used FOC method, where ω_e^{req} is the required rotor speed and θ_I^{req} is the required current angle between the current vector $\boldsymbol{i}_{dq}$ and rotor position $\hat{\theta}_e$. Algorithms, which would utilize the estimated parameters $\hat{K}_m$, $\hat{L}_d$, and $\hat{L}_q$ to optimize efficiency via angle θ_I^{req} are available in the existing literature and are not within the scope of this article [11], [12].

A.　Modified PWM Switching Scheme

The goal of the modified switching scheme is to maximize the duration of the nonzero voltage vectors $\boldsymbol{T}_{vM}$ so that the Δi_{dc} measurement can be taken on at least one phase, no matter the duty cycle $\boldsymbol{D}_{abc}$ value. The principle of the switching scheme is shown in Fig. 4. Calculation of phase duty cycles $\boldsymbol{D}_{abc}$ remains unchanged compared to the standard SVM method. Edge alignment is, however, swapped in every third PWM cycle consequently in each phase. This will not affect the final generated fundamental voltage vector $\boldsymbol{u}_{\alpha\beta}$, but each of the six nonzero voltage vectors $\boldsymbol{v}_M$ is now aligned to either the beginning or the
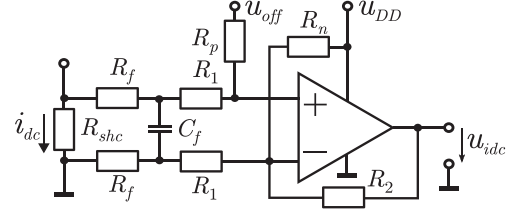
end of the PWM period once during the span of three PWM cycles. This maximizes the periods $\boldsymbol{T}_{vM}$, which serve as Δi_{dc} measurement windows.

B.　Current Derivative Measurement Method

Existing algorithms, which rely on current derivative measurement, usually extract this information from the circuit formed by shunt resistors R_{sh} and the measurement circuit of the phase currents $\boldsymbol{i}_{abc}$ (MC IABC) block (differential operational amplifier) in Fig. 2. The scale of this circuit $\max(\boldsymbol{i}_{abc})$ is, however, set to measure the full range of nominal phase current I_{nom}, which in combination with the large stator inductances of the SynRM makes an accurate Δi_{dc} measurement difficult.

The proposed method shown in Fig. 2 is based on the separate measurement circuit of current Δi_{dc} (MC IDC) with the common shunt resistor R_{shc}, the ADC for u_{idc} signal measurement and the DAC, which generates the u_{off} signal. A schematic diagram of the MC IDC is shown in Fig. 5. It functions as a differential amplifier with a high analog gain of i_{dc} measurement (it has a small scale $\max(i_{dc}) \ll \max(\boldsymbol{i}_{abc})$) and with a floating offset, controlled by signal u_{off}. The u_{off} is adjusted online so that the ADC measurable range $0\,\text{V} < u_{idc} < u_{DD}$ is always maintained. The steady-state operation of the MC IDC can be described as

$$u_{idc} = K_R R_p R_{shc} i_{dc} + K_R R'_1 u_{off} - \frac{R_2}{R_n} u_{DD} \quad (8)$$

where

$$K_R = \frac{R'_1 R_2 + R'_1 R_n + R_2 R_n}{(R'_1 + R_p) R'_1 R_n} \quad (9)$$

and $R'_1 = R_1 + R_f$. Compensation voltage u_{off} is calculated from (8) based on knowledge of the phase currents $\boldsymbol{i}_{abc}$ (obtained using the MC IABC) and the required condition $u_{idc} \simeq u_{DD}/2$. This leads to the linear function

$$u_{off} = \frac{2R_2 + R_n}{2R_n R'_1 K_R} u_{DD} - \frac{R_p R_{shc}}{R'_1} i_N \quad (10)$$

where i_N is the last acquired value of the phase current, which flows via R_{shc} during i_{dc} measurement (for example, $i_N = i_a = i_{dc}$ during T_{v1} and T_{v4}).

An example of the u_{idc} and u_{off} signals in an active system is shown in Fig. 6. Signal u_{off} is updated by the DAC at the beginning of the PWM cycle and when the first switching event occurs. It can be seen that u_{idc} provides good measurement gain and always remains in the valid range during the measurement time window $\boldsymbol{T}_{vM}$.
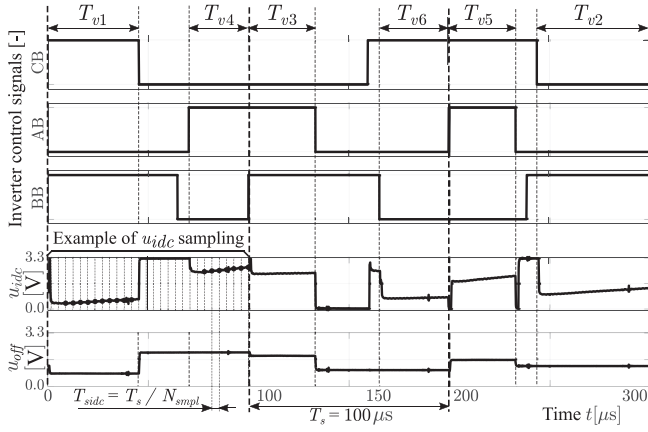
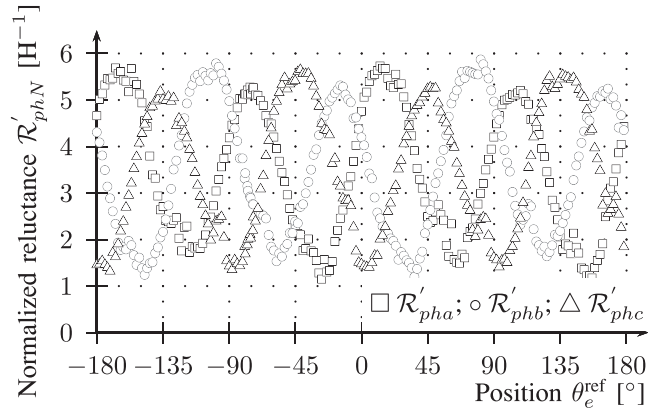Fig. 6. Principle of the proposed i_{dc} current slope measurement.

Fig. 7. Example of $\mathcal{R}'_{phN}$ measurement obtained on a real machine (see Table I).

To acquire the final phase reluctance $\mathcal{R}'_{phN}$ according to (6), the difference $\Delta i_{dc} = \max(i_{dc})\Delta u_{idc}/u_{DD}$ has to be determined. In the proposed algorithm, the signal u_{idc} is sampled equidistantly N_{smpl} times per PWM cycle T_s (see Fig. 6). The acquired data are stored using the DMA to the round buffer and the slope of i_{dc} is obtained using the standard least square algorithm once per T_s. A valid sample set within the buffer is determined using knowledge of the duty cycles $\boldsymbol{D}_{abc}$. An example of the real system measurement of $\mathcal{R}'_{phN}$ dependence on position θ_e for all three phases is shown in Fig. 7. It can be seen that the rotor position, speed, as well as the stator inductances, can be extracted.

C. Extended Kalman Filter

Various position, speed, and parameter estimation methods were proposed for motor drives in the last several decades, however, the EKF is still regarded as a high performing and relevant algorithm. The EKF is the suboptimal state and parameter estimator for nonlinear dynamic systems, which considers the stochastic properties of measurements and estimations. This makes it suitable for the proposed method because the SynRM model (4) is significantly nonlinear and the noisy

phase reluctance $\mathcal{R}'_{phN}$ measurement can be optimally utilized together with more accurate stator current measurement. The disadvantages are relatively high computational demands and a difficult acquisition and description of stochastic properties of measurements and estimated states [27]–[29].

The digital implementation of the estimator is expected, therefore, we first assume the discrete system state-space description

$$\mathbf{x}_{k+1} = \mathbf{f}\left(\mathbf{x}_k, \mathbf{u}_k, \mathbf{w}_k\right)$$
$$\mathbf{y}_k = \mathbf{h}\left(\mathbf{x}_k, \mathbf{v}_k\right) \tag{11}$$

where $\mathbf{x}$ is the state vector, $\mathbf{u}$ is the vector of control variables, $\mathbf{y}$ is the output vector, $\mathbf{w}$ and $\mathbf{v}$ are the process and measurement noise vectors, and $\mathbf{f}$ and $\mathbf{h}$ are nonlinear time-variant system and output functions. Discrete implementation of the extended Kalman filter consists of the prediction step

$$\hat{\mathbf{x}}_{k|k-1} = \mathbf{f}\left(\hat{\mathbf{x}}_{k-1|k-1}, \mathbf{u}_{k-1}, \mathbf{0}\right)$$
$$\mathbf{P}_{k|k-1} = \mathbf{F}_{k-1}\mathbf{P}_{k-1|k-1}\mathbf{F}_{k-1}^T + \mathbf{Q} \tag{12}$$

and the update step

$$\mathbf{K}_k = \mathbf{P}_{k|k-1}\mathbf{H}_k^T \left(\mathbf{H}_k\mathbf{P}_{k|k-1}\mathbf{H}_k^T + \mathbf{R}\right)^{-1}$$
$$\hat{\mathbf{x}}_{k|k} = \hat{\mathbf{x}}_{k|k-1} + \mathbf{K}_k \left[\mathbf{y}_k - \mathbf{h}(\hat{\mathbf{x}}_{k|k-1}, \mathbf{0})\right]$$
$$\mathbf{P}_{k|k} = \left(\mathbf{I} - \mathbf{K}_k\mathbf{H}_k\right)\mathbf{P}_{k|k-1} \tag{13}$$

where $\hat{\mathbf{x}}$ is the state vector estimate, $\mathbf{P}$ is the error covariance matrix, $\mathbf{F}_k$ and $\mathbf{H}_k$ are Jacobians of $\mathbf{f}$ and $\mathbf{h}$, $\mathbf{K}$ is Kalman gain, and $\mathbf{Q}$ and $\mathbf{R}$ are covariance matrices of the process and measurement noise [7], [30]. In our case, the matrices $\mathbf{Q}$ and $\mathbf{R}$ are considered to be constant.

Another major benefit of the EKF is its ability to optimally merge information from multiple measurements based on their stochastic properties. This capability allows us to combine the $\mathcal{R}'_{phN}$ measurement described in Section III-B with the stator flux model (4), so the machine parameter estimation for the power-efficient sensorless operation can be achieved in a wide speed range. This leads to the following state vector:

$$\mathbf{x}_k = \left[\hat{\mathcal{R}}'_d, \quad \hat{\mathcal{R}}'_q, \quad \hat{K}_m, \quad \hat{\Psi}_d, \quad \hat{\Psi}_q, \quad \hat{\omega}_e, \quad \hat{\theta}_e\right]^{\mathrm{T}} \tag{14}$$

and the system input vector

$$\mathbf{u}_k = [u_\alpha, u_\beta]^{\mathrm{T}}. \tag{15}$$

As described in Section III-B, the reluctance of only one phase can be obtained per sampling period T_s. Only one phase reluctance $\mathcal{R}'_{phN}$ will be therefore used in the measurement vector

$$\mathbf{y}_k = \left[\mathcal{R}'_{phN}, \quad i_\alpha, \quad i_\beta\right]^{\mathrm{T}}. \tag{16}$$

Using the Euler discretization method and the flux model (4) and provided that $\hat{K}_m$, $\hat{\mathcal{R}}'_d$, $\hat{\mathcal{R}}'_q$, and $\hat{\omega}_e$ are slow-changing quantities (relative to the sampling period T_s), the nonlinear

time-variant system function is

$$\mathbf{f}\left(\mathbf{x}_k, \mathbf{u}_k, \mathbf{0}\right) = \begin{bmatrix} \hat{\mathcal{R}}'_d \\ \hat{\mathcal{R}}'_q \\ \hat{K}_m \\ \hat{\Psi}_d + T_s(u_d + \hat{\omega}_e \hat{\Psi}_q - R\hat{\mathcal{R}}'_d \Gamma_d A^{-1}) \\ \hat{\Psi}_q + T_s(u_q - \hat{\omega}_e \hat{\Psi}_d - R\hat{\mathcal{R}}'_q \Gamma_q A^{-1}) \\ \hat{\omega}_e \\ \hat{\theta}_e + T_s \hat{\omega}_e \end{bmatrix} \quad (17)$$

where $\Gamma_d = \hat{\Psi}_d - \hat{K}_m \hat{\mathcal{R}}'_q \hat{\Psi}_q$ and $\Gamma_q = \hat{\Psi}_q + \hat{K}_m \hat{\mathcal{R}}'_d \hat{\Psi}_d$.

The nonlinear output function can be assembled using (5), (2), and well-known inverse Park's transformation as

$$\mathbf{h}(\mathbf{x}_k, \mathbf{0}) = \begin{bmatrix} \hat{\mathcal{R}}'_d \cos^2(\hat{\theta}_e + \theta_{phN}) + \hat{\mathcal{R}}'_q \sin^2(\hat{\theta}_e + \theta_{phN}) \\ (\hat{\mathcal{R}}'_d \Gamma_d \cos\hat{\theta}_e - \hat{\mathcal{R}}'_q \Gamma_q \sin\hat{\theta}_e) A^{-1} \\ (\hat{\mathcal{R}}'_d \Gamma_d \sin\hat{\theta}_e + \hat{\mathcal{R}}'_q \Gamma_q \cos\hat{\theta}_e) A^{-1} \end{bmatrix} \quad (18)$$

where θ_{phN} is the stator phase offset for the $\mathcal{R}'_{phN}$ measurement ($\theta_{pha} = 0$ rad, $\theta_{phb} = 2\pi/3$ rad, and $\theta_{phc} = -2\pi/3$ rad).

The Jacobian of the process matrix (17) is

$$\mathbf{F}_k = \left[\frac{\partial \mathbf{f}}{\partial \mathbf{x}}\right]_{\mathbf{x}=\hat{\mathbf{x}}_{k|k}, \mathbf{u}=\mathbf{u}_k, \mathbf{w}=\mathbf{0}}$$

$$= \begin{bmatrix} 1 & 0 & 0 & 0 & 0 & 0 & 0 \\ 0 & 1 & 0 & 0 & 0 & 0 & 0 \\ 0 & 0 & 1 & 0 & 0 & 0 & 0 \\ F_{41} & F_{42} & F_{43} & F_{44} & F_{45} & F_{46} & F_{47} \\ F_{51} & F_{52} & F_{53} & F_{54} & F_{55} & F_{56} & F_{57} \\ 0 & 0 & 0 & 0 & 0 & 1 & 0 \\ 0 & 0 & 0 & 0 & 0 & T_s & 1 \end{bmatrix} \quad (19)$$

where

$$F_{41} = -T_s R \Gamma_d A^{-2} = -T_s R B_1$$

$$F_{51} = -T_s R \hat{K}_m \hat{\mathcal{R}}'_q \Gamma_d A^{-2} = -T_s R C_1$$

$$F_{42} = T_s R \hat{K}_m \hat{\mathcal{R}}'_d \Gamma_q A^{-2} = -T_s R B_2$$

$$F_{52} = -T_s R \Gamma_q A^{-2} = -T_s R C_2$$

$$F_{43} = T_s R \hat{\mathcal{R}}'_d \hat{\mathcal{R}}'_q (\Gamma_q + \hat{K}_m \hat{\mathcal{R}}'_d \Gamma_d) A^{-2} = -T_s R B_3$$

$$F_{53} = -T_s R \hat{\mathcal{R}}'_d \hat{\mathcal{R}}'_q (\Gamma_d - \hat{K}_m \hat{\mathcal{R}}'_q \Gamma_q) A^{-2} = -T_s R C_3$$

$$F_{44} = 1 - T_s R \hat{\mathcal{R}}'_d A^{-1} = 1 - T_s R B_4$$

$$F_{54} = -T_s(\hat{\omega}_e + R \hat{\mathcal{R}}'_d \hat{\mathcal{R}}'_q \hat{K}_m A^{-1}) = -T_s \hat{\omega}_e - T_s R C_4$$

$$F_{45} = T_s(\hat{\omega}_e + R \hat{\mathcal{R}}'_d \hat{\mathcal{R}}'_q \hat{K}_m A^{-1}) = T_s \hat{\omega}_e - T_s R B_5$$

$$F_{55} = 1 - T_s R \hat{\mathcal{R}}'_q A^{-1} = 1 - T_s R C_5$$

$$F_{46} = T_s \hat{\Psi}_q, \; F_{56} = -T_s \hat{\Psi}_d$$

$$F_{47} = T_s u_q, \text{ and } F_{57} = -T_s u_d. \quad (20)$$

The Jacobian of the output matrix (18) is

$$\mathbf{H}_k = \left[\frac{\partial \mathbf{h}}{\partial \mathbf{x}}\right]_{\mathbf{x}=\hat{\mathbf{x}}_{k|k-1}, \mathbf{v}=\mathbf{0}}$$

$$= \begin{bmatrix} 1 & 0 & 0 \\ 0 & \cos\hat{\theta}_e & -\sin\hat{\theta}_e \\ 0 & \sin\hat{\theta}_e & \cos\hat{\theta}_e \end{bmatrix}$$

$$\times \begin{bmatrix} H_{11} & H_{12} & 0 & 0 & 0 & 0 & H_{17} \\ B_1 & B_2 & B_3 & B_4 & B_5 & 0 & -\Gamma_q C_5 \\ C_1 & C_2 & C_3 & C_4 & C_5 & 0 & \Gamma_d B_4 \end{bmatrix} \quad (21)$$

where

$$H_{11} = \cos^2(\hat{\theta}_e + \theta_{phN})$$

$$H_{12} = \sin^2(\hat{\theta}_e + \theta_{phN})$$

$$H_{17} = 2(\hat{\mathcal{R}}'_q - \hat{\mathcal{R}}'_d)\sin(\hat{\theta}_e + \theta_{phN})\cos(\hat{\theta}_e + \theta_{phN}). \quad (22)$$

Measurements (16) are considered to be uncorrelated, therefore the measurement noise covariance matrix has a form

$$\text{diag}\,(\mathbf{R}) = \left[\sigma^2_{\mathcal{R}_{ph}}, \sigma_i^2, \sigma_i^2\right] \quad (23)$$

where $\sigma_{\mathcal{R}_{ph}}$ and σ_i are standard deviations of phase reluctance $\mathcal{R}'_{phN}$ and $i_{\alpha\beta}$ current measurement. The value of $\sigma_{\mathcal{R}_{ph}}$ must be selected manually by analyzing $\mathcal{R}'_{phN}$ measurements on an actual system. Variance σ_i^2 can be modeled as the ADC discretization error and noise introduced by measurement circuit MC IABC, which yields

$$\sigma_i^2 = \left(\frac{\max(i_{abc})}{\sqrt{12} \cdot 2^{N_{\text{ADC}}}}\right)^2 + \text{EIN}^2 \left(\frac{\max(i_{abc})}{u_{DD}} + \frac{1}{R_{sh}}\right)^2 \quad (24)$$

where $\max(i_{abc})$ is the phase current scale, N_{ADC} is the number of ADC bits, R_{sh} is the shunt resistance, u_{DD} is the maximal ADC measurable voltage, and EIN is the equivalent input noise of the operational amplifier [7], [8], [31].

The process noise matrix is also diagonal, and has the form

$$\text{diag}\,(\mathbf{Q}) = \left[\sigma^2_{\mathcal{R}'_d}, \sigma^2_{\mathcal{R}'_q}, \sigma^2_{K_m}, \sigma^2_{\Psi_d}, \sigma^2_{\Psi_q}, \sigma^2_{\omega_e}, \sigma^2_{\theta_e}\right]. \quad (25)$$

Core loss coefficient $\hat{K}_m$ and reluctance $\hat{\mathcal{R}}'_d$ and $\hat{\mathcal{R}}'_q$ states are considered to be slow-changing parameters and their standard deviations $\sigma_{K_m}, \sigma_{\mathcal{R}'_d}$, and $\sigma_{\mathcal{R}'_q}$ can be selected close or equal to zero. Deviation of the stator flux $\hat{\Psi}_d$ and $\hat{\Psi}_q$ can be modeled by introducing the voltage error σ_u as $\sigma_{\Psi_d} = \sigma_{\Psi_q} = T_s\sigma_u$. Voltage error σ_u is caused by model uncertainties at a given U_{dc} and has to be determined experimentally, but usually takes a value of several volts. Speed estimation deviation can be selected as the maximal electrical speed change of moment of inertia J, with nominal torque T_{nom} per sampling period T_s, as $\sigma_{\omega_e} = T_s T_{\text{nom}}/J$. Because position θ_e is obtained as a pure integration of ω_e, its deviation will be $\sigma_{\theta_e} = 0$ rad [7], [8].

The covariance matrix $\mathbf{P}_0$ is initialized as diagonal matrix, usually with sufficiently high values, because the confidence in the initial state estimate is low. Taking into account the scales of the estimated states the matrix $\mathbf{P}_0$ can be, for example, initialized
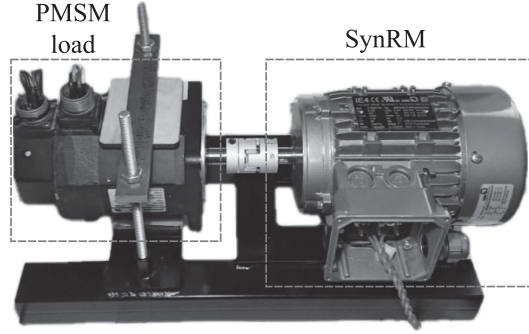
Fig. 8. Experimental setup with a 550 W SynRM.

TABLE I
PARAMETERS OF SynRM

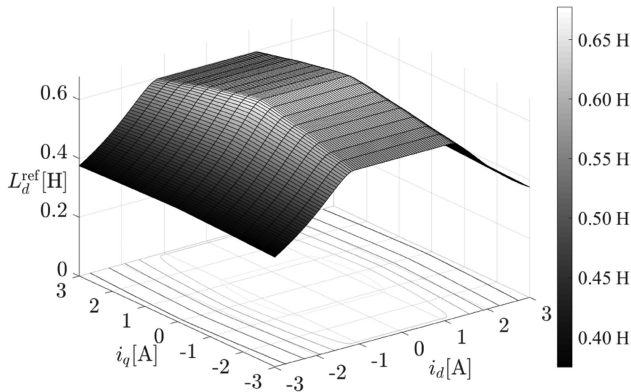| Parameter	Symbol	Value	Unit
Nominal power	P_{nom}	550	W
Nominal speed	N_{nom}	1500	r/min
Nominal voltage	U_{nom}	350	V_{rms}
Nominal current	I_{nom}	1.6	A_{rms}
Nominal torque	T_{nom}	3.5	N·m
Pole pairs	P_p	2	-
Stator resistance	R	9.68	Ω
Moment of inertia	J	$1.64 \cdot 10^{-3}$	kgm^2

Fig. 9. Current dependence of direct axis stator inductance L_d^{ref}.

as

$$\text{diag}\,(\mathbf{P}_0) = \max(\mathbf{x}) \circ \max(\mathbf{x}) \tag{26}$$

where $\max(\mathbf{x})$ is the vector of the maximal expected values that can be reached by the individual states in the vector $\mathbf{x}$.

IV. EXPERIMENTAL RESULTS

The algorithm proposed in this article was implemented on an NXP-MKV58F1M0 Cortex-M7 240 MHz MCU and verified on the experimental setup, with a KSB 550 W SynRM type SuPremE 80M-BWA7F3NRSDWWZWKS (see Fig. 8). Its basic electrical and mechanical parameters are listed in Table I. Offline identification of stator inductances was performed to acquire L_d^{ref} and L_q^{ref} reference inductances, as shown in Figs. 9 and 10 [13].
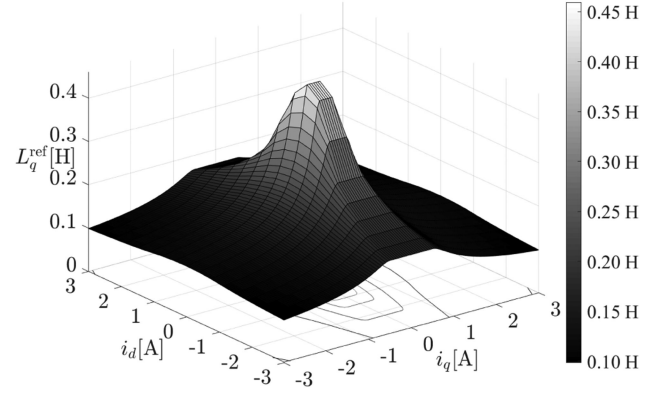

Fig. 10. Current dependency of quadrature axis stator inductance L_q^{ref}.

The initial value of covariance matrix (26) was set based on the previously known motor properties to $\max(\mathcal{R}_d') = 3\,\text{H}^{-1}$, $\max(\mathcal{R}_q') = 5\,\text{H}^{-1}$, $\max(K_m) = 0.1\,\Omega \cdot \text{s/rad}$, $\max(\Psi_d) = 1.0\,\text{Wb}$, $\max(\Psi_q) = 0.3\,\text{Wb}$, $\max(\omega_e) = 314\,\text{rad/s}$, and $\max(\theta_e) = 3.14\,\text{rad}$. Standard deviations of the process noise covariance matrix (25) and the measurement noise covariance matrix (23) were initially set as shown in Section III-C, and then manually tuned. The general rule is that the relative increase of element of the matrix $\mathbf{Q}$ signifies heavier system noise or state uncertainty, leading to the increased Kalman gain $\mathbf{K}$ and faster filter dynamics. Likewise, increasing the relative size of the matrix $\mathbf{R}$ elements leads to the lower confidence in the measurement, signifying the presence of noise and thus lowering the Kalman gain $\mathbf{K}$. The largest change from the initial setup were increased deviations $\sigma_{\mathcal{R}_d'}$, $\sigma_{\mathcal{R}_q'}$, σ_{K_m}, σ_{Ψ_d}, and σ_{Ψ_q}, as the original filter dynamics did not suffice for the set of selected experiments. The final configuration was chosen as

$$\begin{aligned}
\sigma_{\mathcal{R}_{ph}} &= 0.16\,\text{H}^{-1}, & \sigma_i &= 15\,\text{mA} \\
\sigma_{\mathcal{R}_d'} &= 3.2 \cdot 10^{-4}\,\text{H}^{-1}, & \sigma_{\mathcal{R}_q'} &= 3.2 \cdot 10^{-4}\,\text{H}^{-1} \\
\sigma_{K_m} &= 3.2 \cdot 10^{-5}\,\Omega\,\text{s/rad}, & \sigma_{\Psi_d} &= 7.8 \cdot 10^{-3}\,\text{Wb} \\
\sigma_{\Psi_q} &= 7.8 \cdot 10^{-3}\,\text{Wb}, & \sigma_{\omega_e} &= 0.21\,\text{rad/s} \\
\sigma_{\theta_e} &= 0\,\text{rad}.
\end{aligned}$$

As can be seen in Fig. 6, the phase currents of the SynRM used are deformed shortly after a switching event, and therefore a certain number of samples must be discarded first. This is a result of the significant winding length and thus its capacitance, which is necessary to achieve inductance in the range of hundreds of mH. The number of i_{dc} samples per period T_s was selected to $N_{\text{smpl}} = 45$.

In order to achieve high-speed and high-torque regions, voltage injection had to be conducted at high duty cycle levels. This is due to the fact that the stator voltage vector is normally roughly perpendicular to the direct axis. While $\mathcal{R}_{phN}'$ measurement would suffice for the position and speed estimation, identification of inductance $\hat{L}_d$ would be inaccurate.

No advanced efficiency optimization algorithm was used during experiments, and the current angle was set $\theta_I = 45°$.
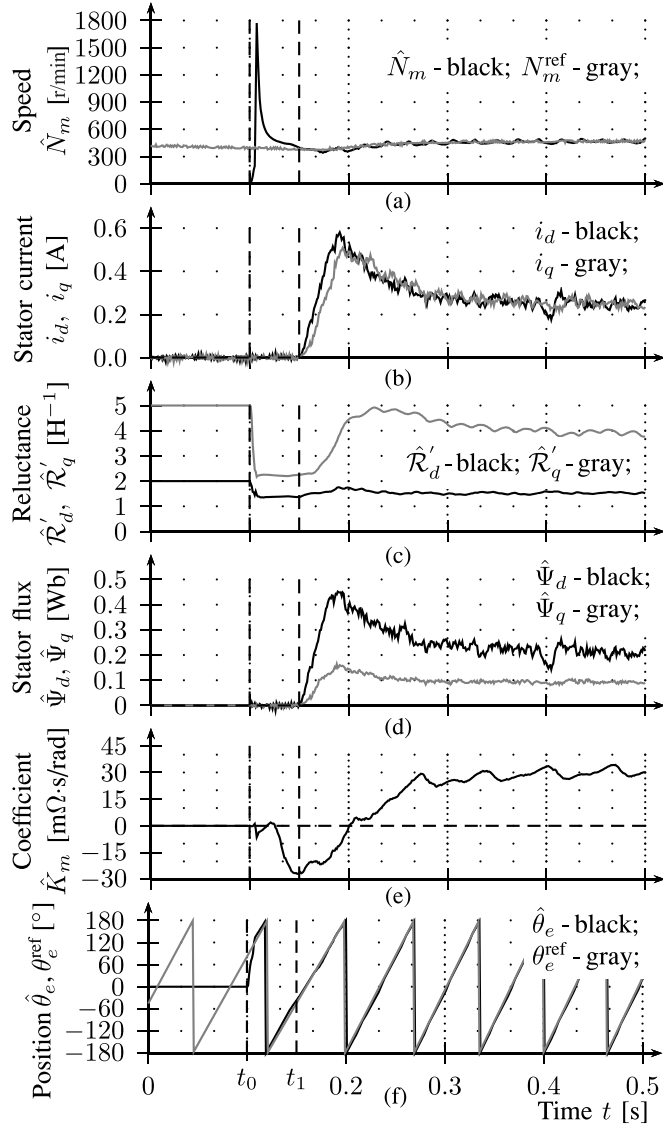
Fig. 11.   On-the-fly EKF startup at t_0 and switch to closed loop at t_1.
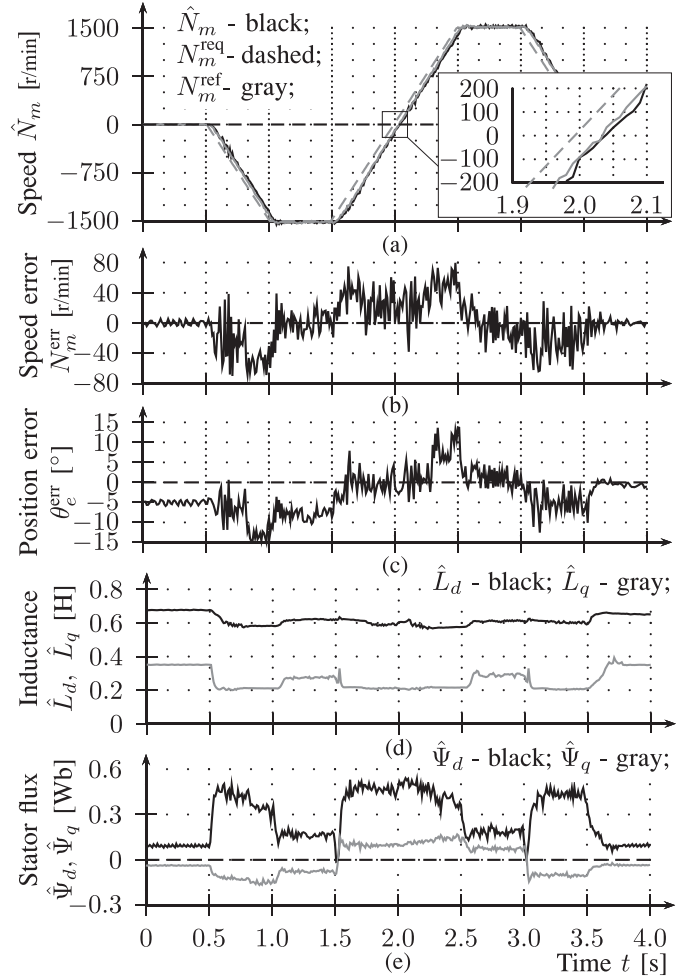

Fig. 12.   (a) and (b) speed $\hat{N}_m$, (c) position $\hat{\theta}_e$, (d) inductance $\hat{L}_d$, $\hat{L}_q$, and (e) flux $\hat{\Psi}_d$, $\hat{\Psi}_q$, estimations in full speed range.

The EKF states and the stator current $\boldsymbol{i}_{dq}$ during the on-the-fly start are shown in Fig. 11. The observer is started at time $t_0 = 100\,\mathrm{ms}$ and switched to closed-loop at $t_1 = 150\,\mathrm{ms}$ with the required speed command set to $N_m^{\mathrm{req}} = 500\,\mathrm{r/min}$. The reference position θ_e^{ref} and speed N_m^{ref} were obtained using the encoder sensor. The measurement demonstrates the behavior with the initial position error $\theta_e^{\mathrm{err}} = \theta_e^{\mathrm{ref}} - \hat{\theta}_e$ close to the worst-case value $\pi/2$. It can be seen that, thanks to the phase reluctance $\mathcal{R}'_{phN}$ measurement, no excitation apart from the proposed PWM switching scheme described in Section III-A is necessary, which allows a smooth on-the-fly startup. This is an advantage when compared to the commonly used HFI and EMF-based SynRM algorithms [15]–[20].

The mechanical speed estimation $\hat{N}_m = 60\hat{\omega}_e/(2\pi P_p)$ in response to the reversal of the required speed N_m^{req} from negative to positive nominal value is shown in Fig. 12. This test demonstrates the full-speed range capability and dynamic performance of the proposed algorithm. The position error θ_e^{err} and the speed

error $N_m^{\mathrm{err}} = N_m^{\mathrm{ref}} - \hat{N}_m$ increased up to 15° and 70 r/min during the acceleration phase, more specifically when the injection started. The missing $\hat{\omega}_e$ mechanical model in the system function (17) also contributed to the estimated speed $\hat{N}_m$ lag, which can also be seen in the detail of speed reversal in Fig. 12(a). To achieve the full speed range, the hybrid algorithms are usually employed. For example, a similar experiment was done in [21] with the hybrid algorithm on 3-kW SynRM machine, showing comparable performance. However, unlike the proposed algorithm, it requires a fusion of position and speed estimates from two separate algorithms.

The startup from stand-still under full nominal load $T_l = 3.5\,\mathrm{N\cdot m}$ with the proposed algorithm is shown in Fig. 13 and the dynamic response to the full nominal load T_l step at $N_m^{\mathrm{req}} = 500\,\mathrm{r/min}$ is shown in Fig. 14. The position error θ_e^{err} reaching up to 17° is similar to the values obtained by experiments with already proposed methods [18], [21], [32], however, superior performance was demonstrated in [16] and [33]. The position error θ_e^{err} peaked during speed and torque dynamic changes, which is also visible as $\hat{L}_d$ and $\hat{L}_q$ inductance
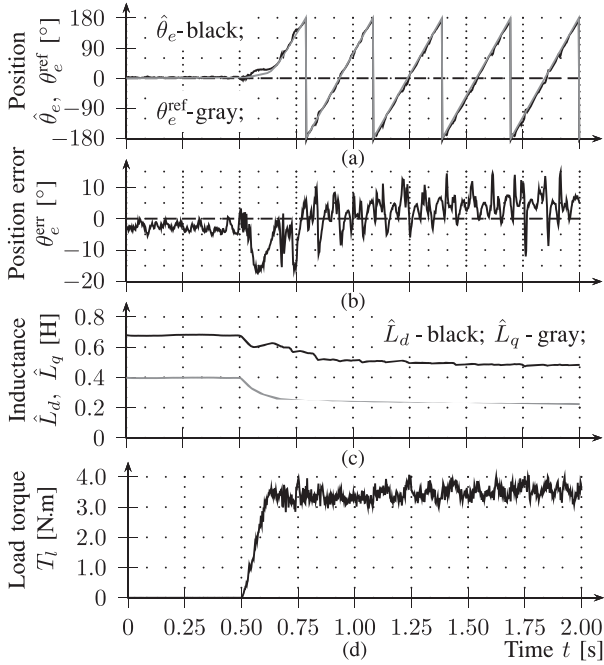
Fig. 13. (a) and (b) position $\hat{\theta}_e$, (c) inductance $\hat{L}_d$, $\hat{L}_q$, estimation during startup under (d) nominal load torque $T_l = 3.5$ N·m.
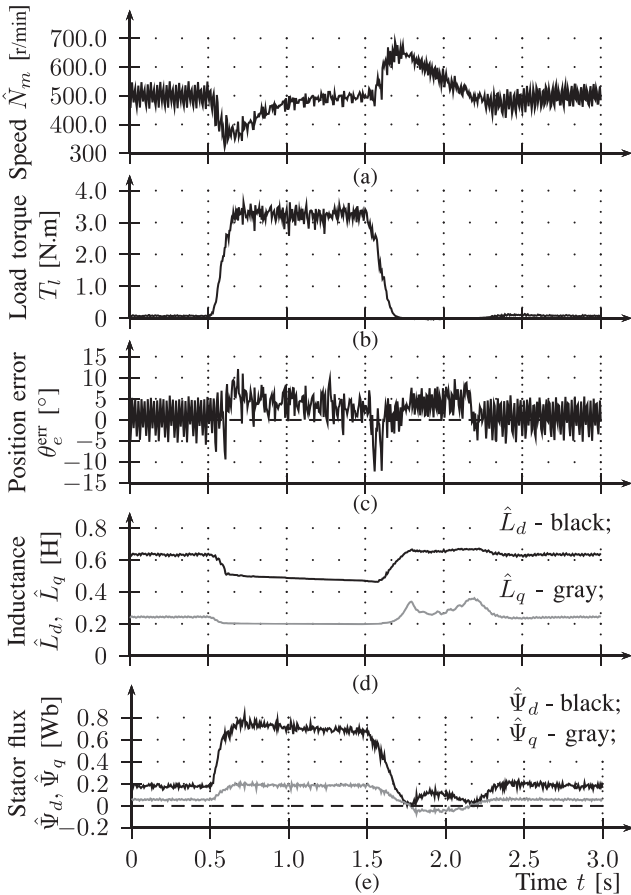

Fig. 14. Nominal load $T_l = 3.5$ N·m, (b) step response of (a) speed $\hat{N}_m$, (c) position $\hat{\theta}_e$, (d) inductance $\hat{L}_d$, $\hat{L}_q$, and (e) flux $\hat{\Psi}_d$, $\hat{\Psi}_q$.
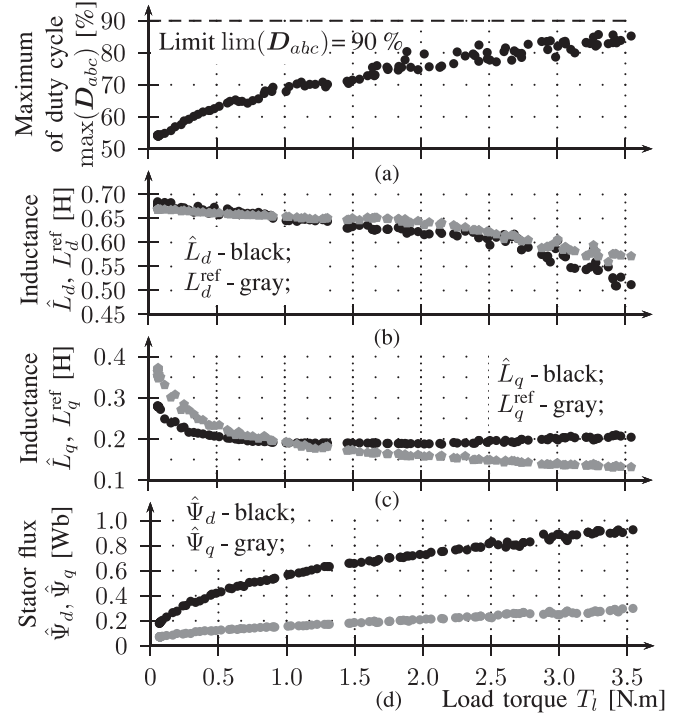

Fig. 15. Load characteristics of (a) duty cycle maximum $\max(D_{abc})$, (b) inductance $\hat{L}_d$, (c) inductance $\hat{L}_q$, and (d) stator fluxes $\hat{\Psi}_d$ and $\hat{\Psi}_q$.

estimation disturbances, however, the steady-state position error θ_e^{err} mostly stayed below $10°$.

All the previous dynamic tests showed an average performance during speed and load changes. As discussed in the introductory section of this article, the SynRM is, however, mostly utilized in less dynamic applications. Therefore, the steady-state performance was investigated. Full nominal torque range characteristics were acquired for direct and quadrature inductances [results in Fig. 15(b) and (c)], and stator fluxes $\hat{\Psi}_d$ and $\hat{\Psi}_q$ [shown in Fig. 15(d)]. While direct axis inductance $\hat{L}_d$ had generally a good match with reference value L_d^{ref}, the quadrature inductance showed an increasing error. This behavior is believed to be a result of negligence of the stator resistance in (6), which results in a small $\mathcal{R}'_{phN}$ deformation (can be also seen in Fig. 7). The maximal actual value of the applied phase duty cycles $\max(\boldsymbol{D}_{abc})$ is in Fig. 15(a). It can be seen that the algorithm can operate close to the duty cycle limit $\lim(\boldsymbol{D}_{abc}) = 90\%$, where the stator voltage maximum is nearly reached.

The speed characteristics of the core losses coefficient $\hat{K}_m$ at no load is shown in Fig. 16. For illustration, the formula

$$\hat{P}_c = \frac{3}{2}\hat{\mathcal{R}}'_d\hat{\mathcal{R}}'_q\hat{K}_m\hat{\omega}_e\left(\hat{\Psi}_d^2 + \hat{\Psi}_q^2\right) \tag{27}$$

was used to convert the estimated coefficient $\hat{K}_m$ to core power losses $\hat{P}_c$ [25]. It can be seen that $\hat{K}_m$ shows a deformation at low speed, however, due to the low value of overall core losses in this speed region, the impact is considered to be negligible.

Overall, the experimental results demonstrate the viability and performance of the proposed online adaptive observer algorithm.
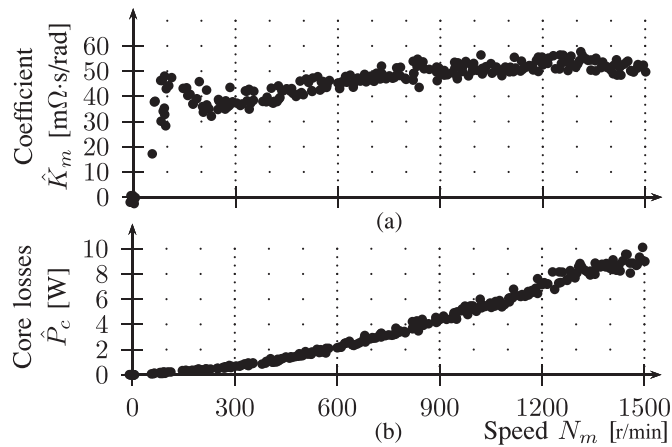
Fig. 16.　Speed characteristics of (a) coefficient $\hat{K}_m$ and (b) core power losses $\hat{P}_c$.

V. Conclusion

This article proposed a novel online adaptive observer algorithm for the SynRM, which can provide the position and speed information required for sensorless operation, as well as the inductance and core loss estimations necessary for power efficiency optimization. Experimental results showed that the algorithm can operate from standstill to the available voltage limit condition without the need of switching between separate low- and high-speed algorithm. Future research will focus on the compensation of stator resistance effect in the phase reluctance measurement, stator resistance estimation, cooperation with an efficiency optimization algorithm, improvement of computational demands, and audible noise reduction.

References

[1] C. Oprea, A. Dziechciarz, and C. Martis, "Comparative analysis of different synchronous reluctance motor topologies," in *Proc. IEEE 15th Int. Conf. Environ. Elect. Eng.*, Jun. 2015, pp. 1904–1909.

[2] H. Liu and J. Lee, "Optimum design of an IE4 line-start synchronous reluctance motor considering manufacturing process loss effect," *IEEE Trans. Ind. Electron.*, vol. 65, no. 4, pp. 3104–3114, Apr. 2018.

[3] V. Kazakbaev, V. Prakht, V. Dmitrievskii, S. Sarapulov, and D. Askerov, "Comparison of power consumption of synchronous reluctance and induction motor drives in a 0.75 kW pump unit," in *Proc. Int. Siberian Conf. Control Commun.*, Jun. 2017, pp. 1–6.

[4] A. J. Piña and L. Xu, "Comparison of apparent power consumption in synchronous reluctance and induction motor under vector control," in *Proc. IEEE Transp. Electrific. Conf. Expo.*, Jun. 2015, pp. 1–6.

[5] A. V. Zakharov, S. I. Malafeev, and A. L. Dudulin, "Synchronous reluctance motor: Design and experimental research," in *Proc. Int. Conf. Elect. Power Drive Syst.*, Oct. 2018, pp. 1–4.

[6] F. Oliveira and A. Ukil, "Comparative performance analysis of induction synchronous reluctance motors in chiller systems for energy efficient buildings," *IEEE Trans. Ind. Informat.*, vol. 15, no. 8, pp. 4384–4393, Aug. 2019.

[7] J. Antons and T. Rösmann, "Self-sensing control of a synchronous reluctance machine using an extended Kalman filter," in *Proc. IEEE Int. Conf. Ind. Technol.*, Mar. 2015, pp. 831–839.

[8] S. Beineke, J. Schirmer, J. Lutz, H. Wertz, A. Bähr, and J. Kiel, "Implementation and applications of sensorless control for synchronous machines in industrial inverters," in *Proc. 1st Symp. Sensorless Control Elect. Drives*, Jul. 2010, pp. 64–71.

[9] Z. Qu and M. Hinkkanen, "Loss-minimizing control of synchronous reluctance motors—A review," in *Proc. IEEE Int. Conf. Ind. Technol.*, Feb. 2013, pp. 350–355.

[10] F. Lin, M. Huang, S. Chen, and C. Hsu, "Intelligent maximum torque per ampere tracking control of synchronous reluctance motor using recurrent Legendre fuzzy neural network," *IEEE Trans. Power Electron.*, vol. 34, no. 12, pp. 12080–12094, Dec. 2019.

[11] Z. Qu, T. Tuovinen, and M. Hinkkanen, "Minimizing losses of a synchronous reluctance motor drive taking into account core losses and magnetic saturation," in *Proc. 16th Eur. Conf. Power Electron. Appl.*, Aug. 2014, pp. 1–10.

[12] H. Hadla and S. Cruz, "Predictive stator flux and load angle control of synchronous reluctance motor drives operating in a wide speed range," *IEEE Trans. Ind. Electron.*, vol. 64, no. 9, pp. 6950–6959, Sep. 2017.

[13] N. Bedetti, S. Calligaro, and R. Petrella, "Stand-still self-identification of flux characteristics for synchronous reluctance machines using novel saturation approximating function and multiple linear regression," *IEEE Trans. Ind Appl.*, vol. 52, no. 4, pp. 3083–3092, Jul. 2016.

[14] M. Hinkkanen, P. Pescetto, E. Mölsä, S. E. Saarakkala, G. Pellegrino, and R. Bojoi, "Sensorless self-commissioning of synchronous reluctance motors at standstill without rotor locking," *IEEE Trans. Ind Appl.*, vol. 53, no. 3, pp. 2120–2129, May 2017.

[15] S. Bolognani, L. Ortombina, F. Tinazzi, and M. Zigliotto, "Model sensitivity of fundamental-frequency-based position estimators for sensorless PM and reluctance synchronous motor drives," *IEEE Trans. Ind. Electron.*, vol. 65, no. 1, pp. 77–85, Jan. 2018.

[16] C. Li, G. Wang, G. Zhang, D. Xu, and D. Xiao, "Saliency-based sensorless control for SynRM drives with suppression of position estimation error," *IEEE Trans. Ind. Electron.*, vol. 66, no. 8, pp. 5839–5849, Aug. 2019.

[17] M. Nikowitz, M. Hofer, and M. Schroedl, "Improvements on a sensorless controlled synchronous reluctance machine down to standstill," in *Proc. Int. Exhib. Conf. Power Electron., Intell. Motion, Renewable Energy Energy Manage.*, Jun. 2018, pp. 1–7.

[18] L. Alberti, O. Bottesi, S. Calligaro, P. Kumar, and R. Petrella, "Self-adaptive high-frequency injection based sensorless control for IPMSM and SynRM," in *Proc. IEEE Int. Symp. Sensorless Control Elect. Drives*, Sep. 2017, pp. 97–102.

[19] M. Hinkkanen, S. E. Saarakkala, H. A. A. Awan, E. Mölsä, and T. Tuovinen, "Observers for sensorless synchronous motor drives: Framework for design and analysis," *IEEE Trans. Ind Appl.*, vol. 54, no. 6, pp. 6090–6100, Nov. 2018.

[20] S. Ichikawa, M. Tomita, S. Doki, and S. Okuma, "Sensorless control of synchronous reluctance motors based on extended EMF models considering magnetic saturation with online parameter identification," *IEEE Trans. Ind Appl.*, vol. 42, no. 5, pp. 1264–1274, Sep. 2006.

[21] F. Oliveira, D. Cavaleiro, R. Branco, H. Hadla, and S. Cruz, "An encoderless high-performance synchronous reluctance motor drive," in *Proc. IEEE Int. Conf. Ind. Technol.*, Mar. 2015, pp. 2048–2055.

[22] F. J. W. Barnard, W. T. Villet, and M. J. Kamper, "Hybrid active-flux and arbitrary injection position sensorless control of reluctance synchronous machines," *IEEE Trans. Ind Appl.*, vol. 51, no. 5, pp. 3899–3906, Sep. 2015.

[23] T. Hatanaka, T. Mabuchi, M. Tomita, M. Hasegawa, S. Doki, and S. Kato, "Robust position sensorless control against inductance variations of synchronous reluctance motors in low-speed region using high-frequency current control," in *Proc. 13th Int. Conf. Elect. Mach.*, Sep. 2018, pp. 1677–1683.

[24] R. Raja, T. Sebastian, and M. Wang, "Online stator inductance estimation for permanent magnet motors using PWM excitation," *IEEE Trans. Transp. Electrific.*, vol. 5, no. 1, pp. 107–117, Mar. 2019.

[25] T. Senjyu, K. Kinjo, N. Urasaki, and K. Uezato, "High efficiency control of synchronous reluctance motors using extended Kalman filter," *IEEE Trans. Ind. Electron.*, vol. 50, no. 4, pp. 726–732, Aug. 2003.

[26] I. Jlassi and A. J. Marques Cardoso, "Model predictive current control of synchronous reluctance motors, including saturation and iron losses," in *Proc. Int. Conf. Elect. Mach.*, Sep. 2018, pp. 1598–1603.

[27] F. Auger, M. Hilairet, J. M. Guerrero, E. Monmasson, T. Orlowska-Kowalska, and S. Katsura, "Industrial applications of the Kalman filter: A review," *IEEE Trans. Ind. Electron.*, vol. 60, no. 12, pp. 5458–5471, Dec. 2013.

[28] X. Li and R. Kennel, "Comparison of state-of-the-art estimators for electrical parameter identification of PMSM," in *Proc. IEEE Int. Symp. Predictive Control Elect. Drives Power Electron.*, May 2019, pp. 1–6.

[29] O. Benjak and D. Gerling, "Review of position estimation methods for IPMSM drives without a position sensor part II: Adaptive methods," in *Proc. XIX Int. Conf. Elect. Mach.*, Sep. 2010, pp. 1–6.

[30] G. Welch and G. Bishop, "An Introduction to the Kalman Filter," Chapel Hill, NC, USA, Tech. Rep. TR 95-041, 1995.

[31] B. Carter and R. Mancini, *Op Amps for Everyone*, 5th ed. Oxford, U.K.: Newnes, 2018.

[32] R. Antonello, L. Ortombina, F. Tinazzi, and M. Zigliotto, "Enhanced low-speed operations for sensorless anisotropic PM synchronous motor drives by a modified back-EMF observer," *IEEE Trans. Ind. Electron.*, vol. 65, no. 4, pp. 3069–3076, Apr. 2018.

[33] M. Bugsch and B. Piepenbreier, "Bandwidth extending approach for sensorless control of synchronous reluctance machines using an HF square-wave-shaped-voltage-injection-based method for low speed range," in *Proc. Int. Symp. Power Electron., Elect. Drives, Autom. Motion*, Jun. 2018, pp. 1239–1244.

Pavel Vaclavek (Senior Member, IEEE) received the M.Sc. and Ph.D. degrees in cybernetics from the Brno University of Technology, Brno, Czech Republic, in 1993 and 2001, respectively. He received the M.Sc. degree in industrial management from Brno University of Technology, Brno, Czech Republic, in 1998.

He is a Research Group Leader with the Central European Institute of Technology, Brno University of Technology. His research interests include advanced control of electrical drives, model predictive control, system modeling and parameters estimation.

Zbynek Mynar (Member, IEEE) received the M.Sc. degree in cybernetics in 2014 from the Brno University of Technology, Brno, Czech Republic, where he is currently working toward the Ph.D. degree.

His research interests include sensorless control of ac electric motors and wireless power transfer. He is an R&D Engineer with NXP Semiconductor N.V., Roznov pod Radhostem, Czech Republic.

Petr Blaha received the M.Sc. and Ph.D. degrees in cybernetics from the Brno University of Technology, Brno, Czech Republic, in 1996 and 2001, respectively.

He is currently a Senior Researcher with the Central European Institute of Technology, Brno University of Technology. His research interests include parameter identification and advanced control of ac electric motors and fault tolerant control of electrical motor drives.